



**HAL**  
open science

## Thermal properties of light nuclei from $12\text{C}+12\text{C}$ fusion-evaporation reactions

L. Morelli, G. Baiocco, M. d'Agostino, F. Gulminelli, M. Bruno, U. Abbondanno, S. Appannababu, S. Barlini, M. Bini, G. Casini, et al.

► **To cite this version:**

L. Morelli, G. Baiocco, M. d'Agostino, F. Gulminelli, M. Bruno, et al.. Thermal properties of light nuclei from  $12\text{C}+12\text{C}$  fusion-evaporation reactions. 2014. hal-00974520v1

**HAL Id: hal-00974520**

**<https://hal.science/hal-00974520v1>**

Preprint submitted on 7 Apr 2014 (v1), last revised 8 Apr 2014 (v2)

**HAL** is a multi-disciplinary open access archive for the deposit and dissemination of scientific research documents, whether they are published or not. The documents may come from teaching and research institutions in France or abroad, or from public or private research centers.

L'archive ouverte pluridisciplinaire **HAL**, est destinée au dépôt et à la diffusion de documents scientifiques de niveau recherche, publiés ou non, émanant des établissements d'enseignement et de recherche français ou étrangers, des laboratoires publics ou privés.

# 1 Thermal properties of light nuclei from $^{12}\text{C}+^{12}\text{C}$ 2 fusion-evaporation reactions

3 L Morelli<sup>1</sup>, G Baiocco<sup>1,2</sup> ‡, M D’Agostino<sup>1</sup>, F Gulminelli<sup>2</sup>,  
4 M Bruno<sup>1</sup>, U Abbondanno<sup>3</sup>, S Appannababu<sup>4</sup>, S Barlini<sup>5,6</sup>,  
5 M Bini<sup>5,6</sup>, G Casini<sup>6</sup>, M Cinausero<sup>4</sup>, M Degerlier<sup>7</sup>,  
6 D Fabris<sup>8</sup>, N Gelli<sup>6</sup>, F Gramegna<sup>4</sup>, V L Kravchuk<sup>4,9</sup>,  
7 T Marchi<sup>4</sup>, A Olmi<sup>6</sup>, G Pasquali<sup>5,6</sup>, S Piantelli<sup>6</sup>, S Valdré<sup>5,6</sup>  
8 and Ad R Raduta<sup>10</sup>

9 <sup>1</sup>Dipartimento di Fisica ed Astronomia dell’Università and INFN, Bologna, Italy

10 <sup>2</sup>LPC (IN2P3-CNRS/Ensicaen et Université), F-14076 Caen cédex, France

11 <sup>3</sup>INFN Trieste, Italy

12 <sup>4</sup>INFN, Laboratori Nazionali di Legnaro, Italy

13 <sup>5</sup>Dipartimento di Fisica ed Astronomia dell’Università, Firenze, Italy

14 <sup>6</sup>INFN Firenze, Italy

15 <sup>7</sup> University of Nevsehir, Science and Art Faculty, Physics Department, Nevsehir,  
16 Turkey

17 <sup>8</sup>INFN, Padova, Italy

18 <sup>9</sup>National Research Center “Kurchatov Institute”, Moscow, Russia

19 <sup>10</sup>NIPNE, Bucharest-Magurele, POB-MG6, Romania

20 E-mail: luca.morelli@bo.infn.it

21 **Abstract.** The  $^{12}\text{C}+^{12}\text{C}$  reaction at 95 MeV has been studied through the complete  
22 charge identification of its products by means of the GARFIELD+RCO experimental  
23 set-up at INFN Laboratori Nazionali di Legnaro (LNL). In this paper, the first of  
24 a series of two, a comparison to a dedicated Hauser-Feshbach calculation allows to  
25 select a set of dissipative events which corresponds, to a large extent, to the statistical  
26 evaporation of highly excited  $^{24}\text{Mg}$ . Information on the isotopic distribution of the  
27 evaporation residues in coincidence with their complete evaporation chain is also  
28 extracted. The set of data puts strong constraints on the behaviour of the level  
29 density of light nuclei above the threshold for particle emission. In particular, a fast  
30 increase of the level density parameter with excitation energy is supported by the data.  
31 Residual deviations from a statistical behaviour are seen in two specific channels, and  
32 tentatively associated with a contamination from direct reactions and/or  $\alpha$ -clustering  
33 effects. These channels are studied in further details in the second paper of the series.

34 PACS numbers: 25.70.z, 24.60.Dr, 27.30.+t, 24.10.Pa

35 *NUCLEAR REACTIONS  $^{12}\text{C}(^{12}\text{C},X)$ ,  $E = 95 \text{ AMeV}$ , Measured Fusion-evaporation  
36 reactions, Observed deviation from statistical behaviour.*

37 Submitted to: *J. Phys. G: Nucl. Phys.*

‡ Present address: Dipartimento di Fisica dell’Università and INFN, Pavia, Italy

## 1. Introduction

The statistical theory of Compound Nucleus (CN) decay is one of the oldest achievements of nuclear physics and has proved its remarkable predictive power since sixty years [1]. Within this theory the detailed output of a generic nuclear reaction is uniquely predicted under the knowledge of nuclear ground state properties and level densities. The knowledge of level densities is not only important for the understanding of nuclear structure [2], but it is also required for different applications of nuclear physics, from nucleosynthesis calculations to reactor science. Its direct measurement from transfer reactions [3] is limited to a relatively low excitation energy domain. Above the thresholds for particle decay, level densities are only accessible in evaporation reactions through the theory of CN decay.

Despite the interest of the issue, mainly inclusive experiments have been used up to now to constrain this fundamental quantity [4], and very few studies exist altogether concerning the evaporation of very light nuclei in the mass region  $A \approx 20$  [5, 6, 7]. However, this mass region is very interesting to explore. Indeed some excited states of different nuclei in this mass region are known to present pronounced cluster structures. These correlations may persist in the ground state along some selected isotopic chains [8], and according to the Ikeda diagrams [9] alpha-clustered excited states are massively expected at high excitation energies close to the multi-alpha decay threshold in all even-even  $N = Z$  nuclei. These cluster structures have been evidenced in constrained density functional calculations [10, 11, 12] close to the threshold energy of breakup into constituent clusters and even beyond. They should lead to exotic non-statistical decays with a privileged break-up into the cluster constituents which start to be identified in the recent literature [13, 14].

Such effects might be experimentally seen as an excess of cluster production with respect to the prediction of the statistical model, provided that the ingredients of the latter are sufficiently constrained via experimental data. It is important to recall that the final inclusive yields represent integrated contributions over the whole evaporation chain. Because of that, the information they bear on specific excitation energy regions of the different nuclei explored during the evaporation process may be model dependent [15] unless the decay chain is fully controlled in a coincidence experiment. To progress on these issues, we have performed an exclusive and complete detection of the different decay products emitted in  $^{12}\text{C}+^{12}\text{C}$  dissipative reactions at 95 MeV. We compared the experimental data to the results of a dedicated Hauser-Feshbach code for the evaporation of light systems (HF $\ell$  from now on) with transmission coefficients and level densities optimized in the  $A \approx 20$  region [16, 17].

In this paper, the first of a series of two, we show that all the observables of dissipative events are fully compatible with a standard statistical behaviour, with the exception of  $\alpha$ -yields in coincidence with Carbon and Oxygen residues.

The good reproduction of a large set of inclusive and exclusive observables by the statistical model allows to constrain the least known part of the theory, namely the

79 behaviour of the level density at high excitation energy, well above the threshold of  
 80 particle decay. We will show that a fast increase of the level density parameter in the  
 81  $A \approx 20$  mass region from  $a \approx 2.4 \text{ MeV}^{-1}$  at the neutron separation energy, to  $a \approx 3.5$   
 82  $\text{MeV}^{-1}$  at  $E^*/A \approx 3 \text{ MeV}$  is compatible with our data.

83 The observed residual anomalies are tentatively attributed to clustering effects  
 84 which appear to survive even in the most dissipative events. These effects will be  
 85 studied in greater detail in the second paper of this series.

## 86 2. The statistical decay code

87 In this section we give the main features of the Monte Carlo HF $\ell$  statistical decay code.  
 88 For further details, see [16].

89 The evaporation of light particles is treated with the standard Hauser-Feshbach (HF)  
 90 formalism of CN decay [18], with n, p, d, t,  $^3\text{He}$ ,  $\alpha$  particles and  $^6\text{Li}$ ,  $^7\text{Li}$  emission  
 91 channels included. The expression for the decay width in channel  $\xi$  for a hot nucleus  
 92  $(A, Z)$  excited in its state  $C$  (specified by the energy  $E^*$  and the angular momentum  
 93  $J$ ), in the framework of the HF model reads:

$$\Gamma_{\xi}^C = \frac{1}{2\pi\rho_C} \int_0^{E^*-Q} d\epsilon_{\xi} \sum_{J_d} \sum_{j=|J-J_d|}^{J+J_d} \sum_{\ell=|j-s_p|}^{j+s_p} T_{j,s_p}^J(\epsilon_{\xi}) \rho_d \quad (1)$$

94 where  $\epsilon_{\xi}$  is the relative kinetic energy of the decay products (the daughter nucleus,  
 95 labeled by  $d$ , and the evaporated particle, labeled by  $p$ );  $Q$  is the decay  $Q$ -value;  $J_d$ ,  $s_p$   
 96 and  $\ell$  are the angular momentum of the daughter nucleus, the spin of the evaporated  
 97 particle and the orbital angular momentum of the decay, respectively and summations  
 98 include all angular momentum couplings between the initial and final states;  $T$  is the  
 99 transmission coefficient;  $\rho_C(E^*, J)$  and  $\rho_d(E^* - Q - \epsilon_{\xi}, J_d)$  are the nuclear Level Density  
 100 (LD) of the decaying and of the residual nucleus, respectively.

101 The widths  $\Gamma_i^C$  are calculated for all possible decay channels and the Branching Ratio  
 102 (BR) associated with a specific channel  $\xi$  is obtained as the ratio between  $\Gamma_{\xi}^C$  and the  
 103 total decay width for the hot nucleus:  $BR^C(\xi) = \Gamma_{\xi}^C / \sum_i \Gamma_i^C$ . This decay probability  
 104 constitutes the main ingredient of the Monte Carlo simulation.

105 In the case of the very light CN studied in this work, simple analytical expressions  
 106 can be safely employed for the transmission coefficients. In our code we have adopted  
 107 the empirical work of [19]:

$$T_{\ell}(\epsilon_{\xi}) = \frac{1}{1 + \exp\left(\frac{V_b - \epsilon_{\xi}}{\delta \cdot V_b}\right)} \quad (2)$$

109 where the barrier  $V_b$  is a sum of a Coulomb and a centrifugal term depending on  $\ell$ ,  
 110 hence on all coupled angular momenta, see (1). Its full expression reads:

$$V_b = \frac{1.44}{r_Z} \frac{Z_p(Z - Z_p)}{(A - A_p)^{1/3} + A_p^{1/3}} + \frac{\hbar^2 \ell(\ell + 1)}{2r_Z^2} \frac{\frac{A}{A_p(A - A_p)}}{\left[(A - A_p)^{1/3} + A_p^{1/3}\right]^2}$$

111 The two free parameters  $\delta$  and  $r_Z$  were optimized to reproduce the decay of discrete  
 112 resonances [19]. They depend on the charge  $Z_p$  of the evaporated particle, and  $\delta$  also  
 113 depends on whether the emission takes place in the sub- or above-barrier region.

114 Concerning the kinematics of the decay with angular momentum, we have adopted  
 115 the semi-classical approach proposed by the GEMINI code [20]. Angular momenta  
 116 are considered as classical vectors, and  $\mathbf{j}_a$  and  $\mathbf{j}_b$  are coupled under the assumption  
 117 of equiprobability for the module of their sum  $\mathbf{j}_s$  between  $|\mathbf{j}_a - \mathbf{j}_b| \leq \mathbf{j}_s \leq |\mathbf{j}_a + \mathbf{j}_b|$ .  
 118 Once the decay channel has been selected, the angular momentum  $J_d$  is obtained  
 119 through a maximization of  $\rho_d(J)$  as a function of  $J$ . Decay  $Q$ -values are calculated  
 120 from experimental binding energies taken from the Audi and Wapstra compilation [21].  
 121 Finally, a special effort has been devoted to the implementation of the level density  
 122 model. In particular, all information on measured excited levels from the online archive  
 123 NUDAT2 [22] has been explicitly and coherently included in the decay calculation.

### 124 2.1. The level density model

125 The back-shifted Fermi gas model (BSFG), with the level density parameter and the  
 126 pairing backshift left as free fit parameters, is known to be a phenomenological approach  
 127 well suited to reproduce the many-body correlated nuclear level density: pairing effects  
 128 are included through the backshift  $\Delta_p$ , and all correlations are taken into account in the  
 129 renormalization of the LD parameter  $a(E^*)$ .

130 In [7] level density parameters for the BSFG model have been determined for a large  
 131 set of nuclei (310 nuclei between  $^{18}\text{F}$  and  $^{251}\text{Cf}$ ), by the fit of complete level schemes  
 132 at low excitation energy and  $s$ -wave neutron resonance spacings at the neutron binding  
 133 energy.

134 In [7], the adopted expression for  $\rho(E^*)$  (after integration on angular momentum  $J$   
 135 and parity  $\pi$ ) reads:

$$136 \quad \rho(E^*) = \frac{\exp[2\sqrt{a(E^* - E_2)}]}{12\sqrt{2}\sigma a^{1/4}(E^* - E_2)^{5/4}} \quad (3)$$

137 where  $\sigma$  is the spin cut-off parameter:

$$138 \quad \sigma^2 = 0.0146A^{5/3} \frac{1 + \sqrt{1 + 4a(E^* - E_2)}}{2a} \quad (4)$$

139 The energy backshift  $\Delta_p = E_2$  is left as the first free parameter in the data fitting.  
 140 The second fit parameter is the asymptotic value  $\tilde{a}$  of the following functional form for  
 141  $a(E^*, Z, N)$  [23]:

$$142 \quad a = \tilde{a} \left[ 1 + \frac{S(Z, N) - \delta E_p}{E^* - E_2} \left( 1 - e^{-0.06(E^* - E_2)} \right) \right] \quad (5)$$

143 where  $S(Z, N) = M_{exp}(Z, N) - M_{LD}(Z, N)$  is a shell correction term,  $M_{exp}$  and  $M_{LD}$   
 144 being respectively the experimental mass and the mass calculated with a macroscopic  
 145 liquid drop formula for the binding energy not including any pairing or shell corrections.  
 146  $\delta E_p$  is a pairing term expressed in terms of the deuteron separation energy. Full details

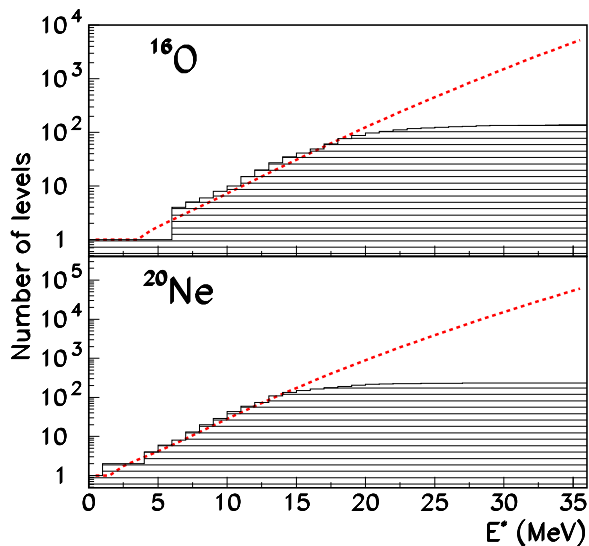


**Figure 1.** Color online: Comparison between the cumulative number of levels given by (3) (lines), and the cumulative counting of experimentally measured levels from the NUDAT2 archive [22] (histograms).

147 on the parameter definition and fit procedure can be found in [7]. As a final result,  
 148 analytic formulas for  $E_2$  and  $\tilde{a}$  as a function of tabulated nuclear properties are given.  
 149 With such formulas for the calculation of LD parameters, the model of (3) allows for  
 150 a very good reproduction of experimental distributions of measured levels in the mass  
 151 region of interest for the present work. Two selected examples are given in Figure 1.  
 152 The isotope  $^{20}\text{Ne}$  belongs to the fitted data set, and the good agreement between the  
 153 line and the histogram shows the quality of the fit procedure of [7]. Concerning  $^{16}\text{O}$ ,  
 154 the values of the parameters are an extrapolation of the formulas proposed in [7] out of  
 155 the fitted data set; from the figure it is also clear that (3) can be considered reliable also  
 156 for nuclei whose level density has not been directly optimized. A similar agreement is  
 157 observed for all the other particle-stable isotopes in the mass region of interest for the  
 158 present study.

159 Still, numerical values for the pairing backshift and for the asymptotic limit of  $a(E^*)$   
 160 with increasing excitation energy obtained through this approach are to be considered  
 161 reliable only up to  $E^*/A \approx 1$  MeV for  $A \approx 20$  nuclei.

162 In particular, it is found that the values of the level density parameter needed to  
 163 reproduce the information on discrete levels are usually lower than the ones coming  
 164 from higher-energy constraints, through the reproduction of data for fusion-evaporation  
 165 or evaporation-after fragmentation studies ( $E^*/A \approx 2 \div 3$  MeV). A functional form  
 166 giving a good reproduction of evaporation spectra at very high excitation energy was

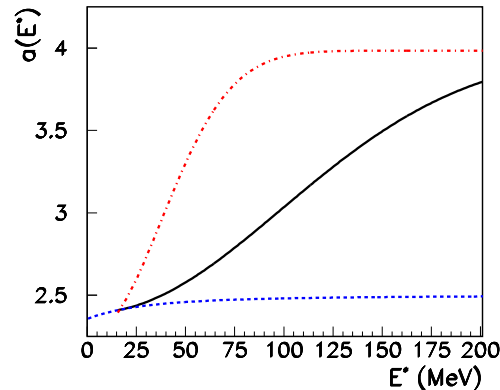


**Figure 2.** (Colour online) Level density parameter calculation for  $^{20}\text{Ne}$ . Blue dashed line: (5). Black solid and red dot-dashed lines: (7) with  $E_l = 8$  and 3 AMeV, respectively.

167 proposed in [24]:

$$168 \quad a_\infty = \frac{A}{14.6} \left( 1 + \frac{3.114}{A^{1/3}} + \frac{5.626}{A^{2/3}} \right) \quad (6)$$

169 To correctly reproduce at the same time the low- and high-energy experimental  
 170 constraints, we have adopted a functional form for the level density parameter that  
 171 gives a continuous interpolation between (5) and (6).

172 We have adopted the following expression:

$$173 \quad a(E^*, A) = \begin{cases} a_D = (5) & \text{if } E^* \leq E_m + E_2 \\ a_C = \alpha \exp[-\beta(E^* - E_2)^2] + a_\infty & \text{if } E^* > E_m + E_2 \end{cases} \quad (7)$$

174 The choice of a rapid (exponential) increase is imposed by the fact that the  
 175 asymptotic value (6) is connected to the opening of the break-up or multifragmentation  
 176 channels, which is a sharp threshold phenomenon. The  $\alpha$  and  $\beta$  parameters are fully  
 177 determined by the matching conditions between the low-energy and high-energy regime:  
 178  $a_D(E_m, A) = a_C(E_m, A)$  and  $a_C(E_l, A) = a_\infty \pm 10\%$ .

179 Here,  $E_l$  represents the limiting energy at which the break-up or fragmentation  
 180 regime is attained, while  $E_m$  is the excitation energy marking the transition between  
 181 the discrete and the continuum part of the spectrum. This latter quantity is of the  
 182 order of  $E_m \approx 10$  MeV, coherently with the value of the critical energy for the damping  
 183 of pairing effects in [25]. In the case of light nuclei for which a large set of measured  
 184 levels is available, this value well corresponds to the excitation energy maximizing the  
 185 number of levels in bins of  $E^*$ . Above  $E_m$  the experimental information is too poor  
 186 to consider the set of resolved levels exhaustive of the nuclear level density, due to the  
 187 physical emergence of the continuum.

188 The limiting energy  $E_l$  is then left as the only free parameter of the calculation,  
 189 governing the rapidity of the variation of  $a(E^*)$  above  $E_m$ . As an example of the overall

190 functional form resulting for the level density parameter, in Figure 2 we plot  $a(E^*, A)$   
 191 for  $^{20}\text{Ne}$ , for two different choices of  $E_l$ .

192 In the statistical code, starting from a given CN  $(A, Z, J, E^*)$ , the decay pattern is  
 193 calculated with the Monte-Carlo technique as a sequence of two-body decays governed  
 194 by the emission probability given by (1). When the emitted particle leaves the daughter  
 195 nucleus at an excitation energy  $E_d^* < E_m$ , the excitation energy is considered as a  
 196 discrete variable, and one of the tabulated levels [22] of the daughter discrete spectrum  
 197 is populated. The level is chosen according to the Breit-Wigner distribution of the  
 198 discrete levels considering their respective widths, including the full spectroscopic  
 199 information of [22], and the particle kinetic energy is adjusted if necessary to ensure  
 200 energy conservation. When a particle bound level is populated, the subsequent decay  
 201 is assumed to be due to a single  $\gamma$  emission to the corresponding ground state. If the  
 202 daughter excitation energy  $E_d^*$  is greater than  $E_m$ , the spectroscopic information is not  
 203 sufficient to fully constrain the spin and energy of the daughter nucleus. If measured  
 204 excited states exist, they are populated with a probability given by the ratio between  
 205 the measured level density from discrete states and the total level density including the  
 206 continuum states and given by (3) with  $a$  given by (7). If no levels are known, the  
 207 emission is assumed to take place in the continuum.

### 208 3. Experiment and data selection

209 The measurement was performed in the third experimental Hall of LNL. The  $^{12}\text{C}+^{12}\text{C}$   
 210 reaction had been already studied in a previous experiment, and first results on the  
 211 persistence of cluster correlations in dissipative reactions highlighted by the comparison  
 212 of the data set with HF $\ell$  calculations were reported [17]. The limited statistics of the  
 213 experiment prevented detailed studies of the breakup angular and energy correlations.  
 214 Here we report the analysis of the new data-taking, which confirms our previous findings  
 215 and additionally allows to study the deviations from statistical behaviour in specific  
 216 channels and in greater detail.

217 A pulsed beam (less than 2 ns FWHM, 400 ns repetition period) of  $^{12}\text{C}$  provided by  
 218 the TANDEM accelerator impinged with a self-supporting  $^{12}\text{C}$  target, with a thickness  
 219 of  $85 \mu\text{g}/\text{cm}^2$ . The bombarding energy was 95 MeV.

#### 220 3.1. The experimental setup

221 The experimental setup is composed by the GARFIELD detector, covering almost  
 222 completely the angular range of polar angles from  $30^\circ$  to  $150^\circ$ , and the Ring-Counter  
 223 (RCo) annular detector [26], centered at  $0^\circ$  with respect to the beam direction and  
 224 covering forward laboratory angles in the range  $5^\circ \leq \theta \leq 17^\circ$ .

225 The combination of the two devices allows for a nearly- $4\pi$  coverage of the solid  
 226 angle, which, combined with a high granularity, permits to measure the charge, the  
 227 energy and the emission angles of nearly all charged reaction products. The setup also



228 provides information on the mass of the emitted charged products in a wide range of  
229 particle energy [27].

230 The GARFIELD apparatus is a two-detection stage device, consisting of two  
231 microstrip gaseous drift chambers ( $\mu\text{SGC}$ ), filled with  $\text{CF}_4$  gas at low pressure (50  
232 mbar) and placed back to back, with  $\text{CsI}(\text{Tl})$  scintillation detectors lodged in the same  
233 gas volume.

234 Due to the small size of the studied system, mainly light particles are emitted in the  
235 reaction which are efficiently detected and identified through the use of the *fast – slow*  
236 shape method for the 180  $\text{CsI}(\text{Tl})$  scintillators [28].

237 The energy identification thresholds result, on average, 3, 6, 9, 20, 7 MeV for  $p$ ,  
238  $d$ ,  $t$ ,  $^3\text{He}$ , and  $\alpha$  particles, respectively. As for other experimental devices using the  
239 *fast – slow* technique [29],  $^3\text{He}$  can be discriminated from  $\alpha$ 's starting from  $\approx 20$  MeV.  
240 This increase of the  $^3\text{He}$  threshold does not affect too much the  $\alpha$  yield in our reaction,  
241 since  $^3\text{He}$  is estimated to represent less than 2-3% of  $Z=2$  particles [17]. In all the  
242 experimental percentages, the associated error takes into account both the statistical  
243 error and the possible  $^3\text{He} - \alpha$  contamination. In the present analysis, the information  
244 coming from the  $\mu\text{SGC}$  has been used to validate the particle identification, especially  
245 in the lower part of the range, where the *fast – slow* curves tend to merge.

246 The RCo detector is an array of three-stage telescopes realized in a truncated  
247 cone shape. The first stage is an ionization chamber (IC), the second a  $300\mu\text{m}$  reverse  
248 mounted Si(nTD) strip detector, and the last a  $\text{CsI}(\text{Tl})$  scintillator.

249 The angular resolution is  $\Delta\theta \approx \pm 0.7^\circ$  and the energy resolution of silicon strips  
250 and  $\text{CsI}(\text{Tl})$  detectors resulted 0.3% and 2-3%, respectively. In the present experiment,  
251 reaction products with  $Z \geq 3$  have relatively low energies and are stopped in the  $\text{Si}$   
252 detectors. Therefore, they can be identified only in charge thanks to the  $\Delta E - E$   
253 correlation between the energy loss in the gas and the residual energy in the silicon  
254 detectors, with 1 AMeV energy threshold. Only for the high energy tails of  $3 \leq Z \leq 5$   
255 fragments mass identification has been possible, thanks to the application of a pulse  
256 shape technique to signals coming from the  $\text{Si}$  detectors [30]. Light charged particles  
257 (LCP,  $Z = 1, 2$ ) flying at the RCo angles and punching through the  $300\mu\text{m}$  Si pads  
258 ( $E/A \geq$  about 6 MeV) are identified in charge and mass by the conventional Si - CsI  
259  $\Delta E - E$  method. LCP stopped in the silicon stage are identified only in charge.

260 More details on this setup can be found in [27].

### 261 3.2. Minimum bias compound nucleus selection

262 The analysis considers only events with a coincidence between at least one LCP, detected  
263 and identified in GARFIELD, and a particle or fragment ( $Z \geq 3$ ) detected at forward  
264 angles in the RCo and identified in charge. In the case of a fusion-evaporation reaction,  
265 this latter is the residue  $Z_{\text{res}}$  of the CN decay chain, and it is expected to have a velocity  
266 close to the center-of-mass velocity of the reaction,  $v_{\text{CM}} \approx 2$  cm/ns. Due to the lack of  
267 isotopic resolution for such low energy fragments, a hypothesis on their mass has to be

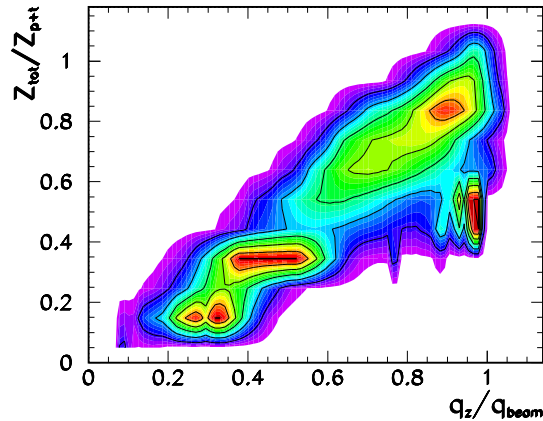


**Figure 3.** Colour online: Contour plot of the total detected charge ( $Z_{tot}$ ) normalized to the sum of the projectile and target charge  $Z_{p+t}$  as a function of the total measured longitudinal momentum ( $q_z$ ) normalized to the projectile momentum ( $q_{beam}$ ).

268 done. Our initial hypothesis (to be further discussed in §4.2) is  $A_{res} = 2 \cdot Z_{res}$ .

269 A first selection within the measured events is based on Figure 3, where we show  
 270 the total detected charge as a function of the total longitudinal momentum. Requiring  
 271 that at least 60% of the total incoming parallel momentum is collected, we obtain a  
 272 total charge distribution centered at  $Z_{tot} = 10$ , corresponding to the 80% of the total  
 273 charge. A yield peak around  $Z_{tot}/Z_{p+t} = 0.5$  is evident in the picture, corresponding  
 274 to (quasi)–elastic events with only the Carbon ejectile detected. Since we would  
 275 like to concentrate on specific decay channels, we would keep a complete detection  
 276 ( $Z_{tot} = 12$ ). We have therefore checked that this stringent requirement does not bias  
 277 the characteristics of the events, comparing the distribution of representative observables  
 278 with a less stringent selection  $Z_{tot} \geq 10$ . Very similar distributions are obtained with the  
 279 two “minimum bias” selections which henceforth we name “quasi-complete” ( $Z_{tot} \geq 10$ )  
 280 and “complete” ( $Z_{tot} = 12$ ) (see § 4.1). Complete events are  $\approx 20\%$  of quasi-complete  
 281 ones.

#### 282 4. Data analysis and comparison to statistical model calculations

283 With the minimum bias event selections discussed in § 3.2, we compare experimental  
 284 data to the predictions of our Monte Carlo Hauser-Feshbach code HF $\ell$  (§2) for the  
 285 evaporation of the CN  $^{24}\text{Mg}$ , at  $E^*/A_{CN} = 2.6$  MeV, issued in case of complete fusion.  
 286 The angular momentum input distribution for the fused system in this reaction can be  
 287 assumed to be a triangular one, with a maximum value  $J_{0\ max} = 12 \hbar$ , coming from  
 288 the systematics [31]. Because of parity conservation, only even values of  $J_0$  extracted  
 289 from the triangular distribution are allowed as an input for the CN angular momentum.  
 290 Finally, code predictions are filtered through a software replica of the experimental set-  
 291 up, taking into account the geometry, the energy thresholds, the energy resolution and

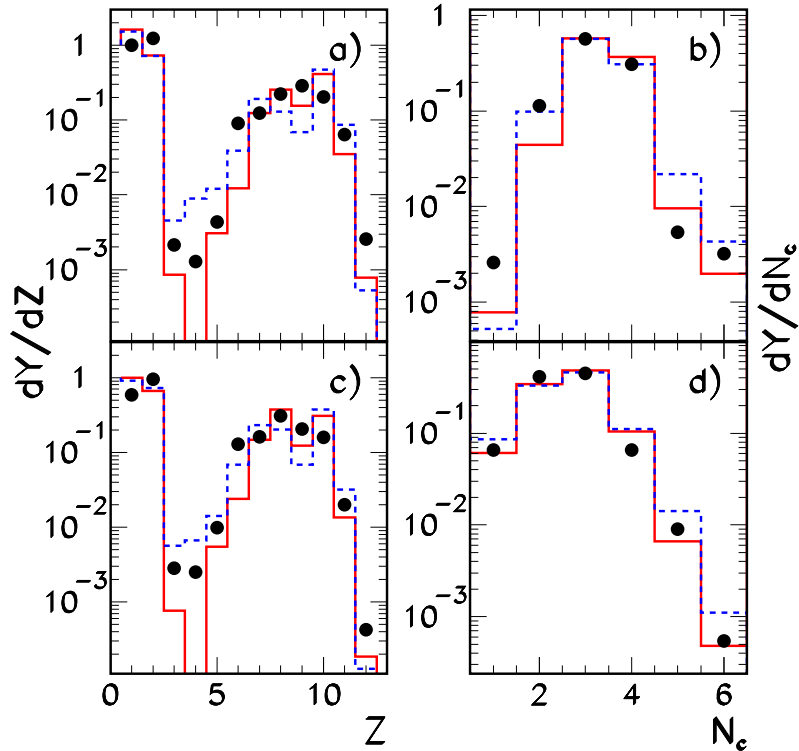


**Figure 4.** Colour online: Measured (symbols) and calculated (histograms) charge and charged particle multiplicity distribution. Panels a), b) refer to complete ( $Z_{tot} = 12$ ) events, panels c), d) to quasi-complete events ( $Z_{tot} \geq 10$ ). The red solid line gives the result of the HF $\ell$  calculation, while the blue dashed line is obtained using the GEMINI++ model. All distributions are normalized to the total number of events.

292 the solid angle for each detector.

293 The comparison of various experimental and simulated observables is used to  
 294 validate the parameterizations of statistical model ingredients implemented in the code.

#### 295 4.1. Experimental observables

296 The inclusive charge and multiplicity distribution of events completely and quasi-  
 297 completely detected in charge are presented in Figure 4 in comparison with the filtered  
 298 HF $\ell$  calculation. In this figure and in the following ones experimental data are always  
 299 shown with statistical error bars, when visible.

300 The charge distribution is globally well-reproduced by the theoretical calculation  
 301 and its overall shape is typical of fusion-evaporation reactions.

302 However, a few discrepancies can be observed. Notably,  $Z = 4$  fragments are absent  
 303 in the Hauser-Feshbach prediction while they are not negligible in the experimental  
 304 sample. This could be interpreted as the presence of a break-up contribution in the data  
 305 which is not properly treated by the sequential calculation. To confirm this statement,  
 306 we show in the same figure the result from a GEMINI++ calculation [20] subject to

307 the same filtering procedure. This model, which has also been largely and successfully  
 308 used by the nuclear physics community since more than 20 years, includes the emission  
 309 of intermediate mass fragments within the transition state formalism. We can see that  
 310 GEMINI++ predicts sizeable yields of the lightest fragments, which in the Hauser-  
 311 Feshbach formalism have a negligible probability to be emitted and are only obtained as  
 312 evaporation residues. In particular, the transition state formalism succeeds in explaining  
 313 the missing Be cross section.

314 Concerning the multiplicity distribution, presented in the right part of Figure 4,  
 315 we can see that both the HF $\ell$  and the GEMINI++ calculations reproduce the data  
 316 satisfactorily. We can however remark that GEMINI++ overpredicts events of high  
 317 multiplicity. This means that the transition state formalism is not entirely satisfactory  
 318 in describing the production of light fragment, which could also be due to a breakup  
 319 mechanism. Such a mechanism is not accounted for in the presented models.

320 Apart from the missing  $Z = 4$  channel, another discrepancy between the HF $\ell$   
 321 calculation and the data concerns the  $Z = 6$  yield which is underestimated by the  
 322 model. This extra yield could in principle be explained by the transition state model,  
 323 as shown by the fact that data are well reproduced in this channel by GEMINI++. As  
 324 an alternative explanation, the Carbon excess with respect to HF $\ell$  predictions could  
 325 be due to the entrance channel of the reaction. Indeed, many other experiments [32]  
 326 where reactions with Carbon projectile and/or target were studied, showed an extra-  
 327 production of Carbon residues with respect to statistical models expectations. At low  
 328 bombarding energy,  $C-C$  quasi-molecular states [32] can be invoked. In our experiment,  
 329 as it will be discussed in the following, this anomaly is essentially associated with the  
 330 specific  $C - 3\alpha$  channel.

331 Because of the great similarity between the HF $\ell$  and GEMINI++ calculations, and  
 332 the fact that the HF $\ell$  code was optimized on light systems (see §2), in the following we  
 333 exclusively use the HF $\ell$  code as a reference statistical model calculation.

334 Due to the low statistics of the experiment for  $Z = 3, 4$  residues, we will not study  
 335 these residue channels any further.

336 The dominant fusion-evaporation character of the reaction is further demonstrated  
 337 in Figure 5, which shows the velocity distributions in the laboratory frame of the  
 338 different fragments with  $Z \geq 5$ . The good reproduction by the statistical model allows  
 339 to interpret these fragments mainly as evaporation residues left over by the decay of  
 340  $^{24}\text{Mg}$  CN originated from complete fusion.

341 A complementary information is shown in Figure 6, which displays the laboratory  
 342 energy spectra of protons and  $\alpha$  particles detected in GARFIELD. Experimental data  
 343 (dots) are compared to model calculations (lines). From now on we will concentrate  
 344 on events with a residue detected in the RCo ( $5^\circ \div 17^\circ$ ) and LCP in GARFIELD  
 345 ( $30^\circ \div 150^\circ$ ) as in the previous experiment [17]. This choice is essentially due to the  
 346 different thresholds on LCP identification in RCo and GARFIELD, as pointed out  
 347 in §3.1. To facilitate the comparison of the spectral shapes, distributions are always  
 348 normalized to the same area.

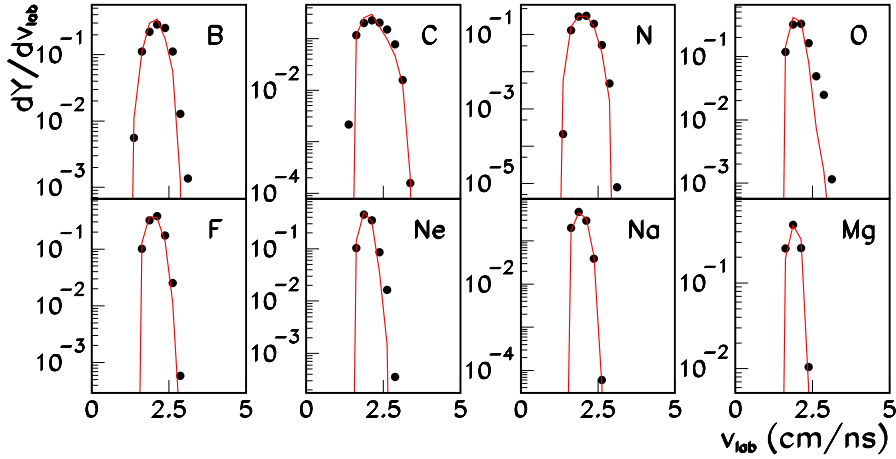


**Figure 5.** (Colour online) Residue laboratory velocity for complete events ( $Z_{tot} = 12$ ) (symbols) in comparison with the HF $\ell$  calculation (lines). All distributions are normalized to unitary area.

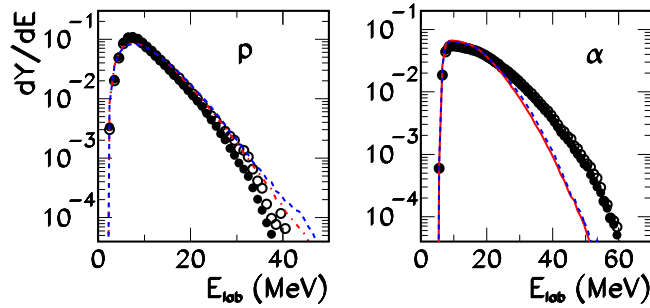


**Figure 6.** (Colour online) Proton (left part) and  $\alpha$  (right part) energy distributions in the laboratory frame, detected in quasi-complete  $Z_{tot} \geq 10$  events (full symbols) and in complete  $Z_{tot} = 12$  events (open symbols). Data (symbols) are compared to model calculations (lines). Red solid lines: quasi-complete  $Z_{tot} \geq 10$  events. Blue dashed lines: complete  $Z_{tot} = 12$  events. All spectra are normalized to unitary area.

349 We can see that the choice of the set of events (complete and quasi-complete) does  
 350 not deform the shape of the spectra. A satisfactory reproduction of the proton energy  
 351 spectrum is achieved, while a large discrepancy in the shape of the distributions appears  
 352 for  $\alpha$  particles for both completeness requirements.

353 Another information can be obtained from angular distributions of protons and  $\alpha$ -  
 354 particles (see Figure 7). The proton distribution is in agreement with the model, while  
 355 the excess of  $\alpha$  particles at backward laboratory angles could suggest a preferential  
 356 alpha emission from the quasi-target. Alternatively, it could indicate an alpha transfer

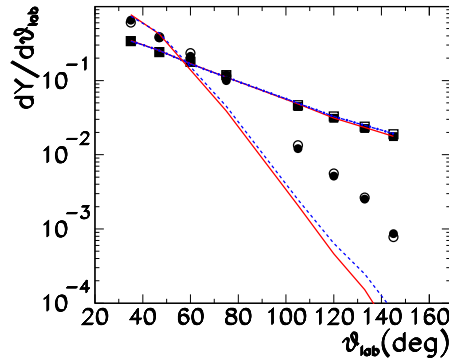


**Figure 7.** (Colour online) Proton (squares) and  $\alpha$  (circles) angular distributions in the laboratory frame, detected in complete  $Z_{tot} = 12$  (open symbols) and in quasi-complete  $Z_{tot} \geq 10$  (full symbols) events. Data (symbols) are compared to model calculations (lines). Blue dashed lines correspond to complete events, red solid lines to quasi-complete events. Experimental and calculated distributions are normalized to unitary area.

357 mechanism from an excited  $^{12}\text{C}$  nucleus with strong alpha correlations.

358 As it is commonly known, the shape of LCP energy spectra is determined by  
 359 the interplay of all physical ingredients entering in the evaporation process, notably  
 360 including transmission coefficients, angular momentum effects and level density [4].  
 361 Nevertheless, when comparing data to statistical model calculations, it is possible to  
 362 try to disentangle the effects of single ingredients [4]. In particular, while transmission  
 363 coefficients define the shape of evaporated spectra in the Coulomb barrier region, the  
 364 level density mostly affects the slope of the exponential tail. Concerning angular  
 365 momentum, the inclusion of deformation has a stronger influence on heavier fragment  
 366 emission, as it is the case for  $\alpha$  particles, and, as a consequence, the tail of the energy  
 367 distribution for such fragments becomes steeper.

368 Thus the two theoretical uncertainties which could be responsible of the observed  
 369 deviations are the estimated maximum angular momentum leading to CN formation,  
 370 and the level density parameter. As we have discussed in § 2, the only unknown in the  
 371 level density is the asymptotic value of the  $a$  parameter at very high excitation energy.  
 372 The effects of a very wide variation of these parameters, including an unrealistically low  
 373 value of  $l_{max}$  and a very high value of  $E_l$  are shown in Figure 8. This figure shows that  
 374 no common choice on the LD parameters can be done in order to reproduce at the same  
 375 time proton and  $\alpha$  energy spectra. For this reason we keep in the rest of the analysis  
 376 the fiducial values  $l_{max} = 12\hbar$ ,  $E_l = 3$  AMeV (red lines).

377 The comparison made so far on many inclusive observables suggests that the  
 378 dominant reaction mechanism is CN formation and the discrepancy found for  $\alpha$  particles  
 379 reflects an out-of-equilibrium emission.

380 A first confirmation of this hypothesis comes from the finding that the largest source

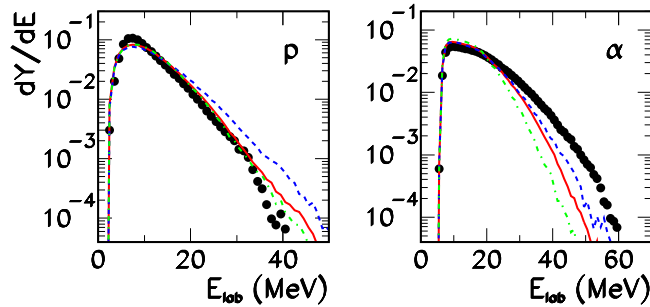


**Figure 8.** (Colour online) Proton (left part) and  $\alpha$  (right part) energy distributions in the laboratory frame, detected in complete events. Data (symbols) are compared to model calculations, with different choices for the assumed maximum angular momentum  $l_{max}$  and limiting energy  $E_l$ . Red solid lines:  $l_{max} = 12\hbar$ ,  $E_l = 3$  A MeV. Blue dashed lines:  $l_{max} = 12\hbar$ ,  $E_l = 8$  A MeV. Green dot-dashed lines:  $l_{max} = 6\hbar$ ,  $E_l = 3$  A MeV. All spectra are normalized to unitary area.

381 of disagreement between data and calculations is for decay channels with  $\alpha$  particles  
 382 detected in coincidence with an Oxygen fragment. This is shown in Figure 9, which  
 383 presents energy spectra of protons and  $\alpha$  particles detected in coincidence with a residue  
 384 of a given atomic number. The discrepancy, larger at the most forward angles [16], is  
 385 mainly due to the 2  $\alpha$ -channel, as we will discuss in § 4.3.

386 With the exception of the  $\alpha - O$  coincidence, particle energy spectra are very well  
 387 reproduced by the statistical model. This gives strong confidence to our level density  
 388 model of (3) and (7) with  $E_l = 3$  A MeV (corresponding to  $a \approx 3.5$  MeV $^{-1}$  for  $E^*/A = 3$   
 389 MeV) for the light  $A \approx 20$  CN decay.

390 A small difference of the experimental and calculated energy spectra is also observed  
 391 for  $\alpha$ -particles in coincidence with a Carbon residue. This does not seem to be related  
 392 to the presence of peripheral events with a Carbon quasi-projectiles, since the velocity  
 393 distribution of Carbon residues (shown in Figure 5) displays a good agreement with  
 394 statistical calculations.

395 The angular distributions of protons and  $\alpha$  particles in coincidence with each residue  
 396 are shown in Figure 10. The good agreement among data and model predictions as  
 397 far as proton distributions are concerned is confirmed. A large discrepancy is evident  
 398 for  $\alpha$  particles at backward laboratory angles detected in coincidence with an Oxygen  
 399 fragment.

400 To understand the origin of the deviations from a statistical behaviour, the  
 401 branching ratios to  $\alpha$  decay and  $\alpha$  kinematics in the different channels involving  $\alpha$   
 402 emission will be studied in greater detail in Section 4.3.

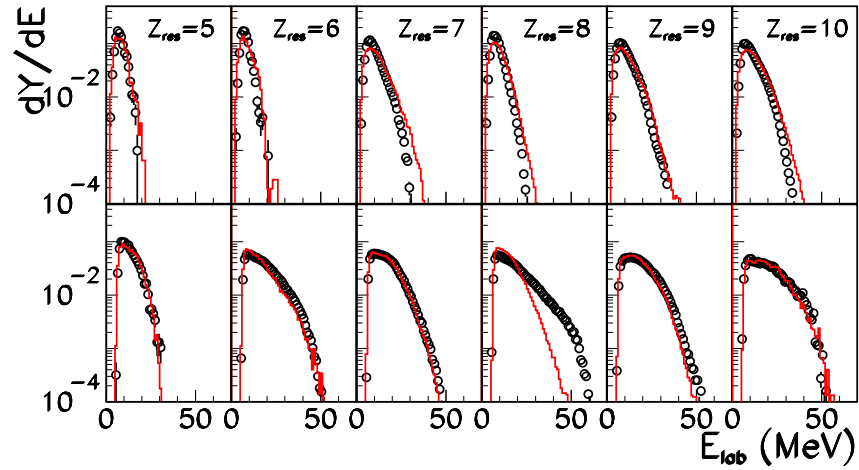


**Figure 9.** (Colour online) Proton (upper part) and  $\alpha$  (lower part) laboratory energy spectra in complete events detected in coincidence with a residue of charge  $Z_{res}$ , indicated in each column. Data (symbols) are compared to model calculations (lines). All spectra are normalized to unitary area.

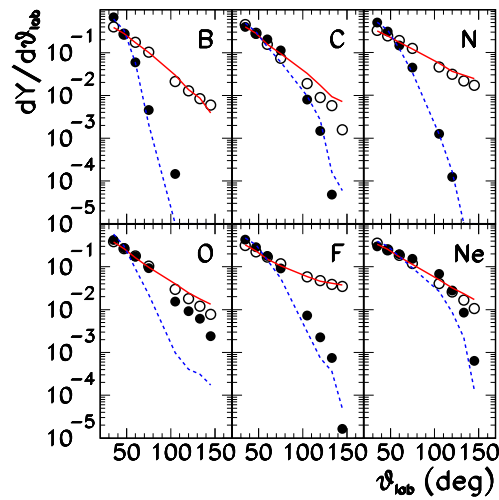


**Figure 10.** (Colour online) Proton (open symbols) and  $\alpha$  (full symbols) angular distributions in the laboratory frame, detected in complete events in coincidence with the indicated residues. Data are compared to model calculations. Red solid lines correspond to protons, blue dashed lines to  $\alpha$ 's. Experimental and calculated distributions are normalized to unitary area.



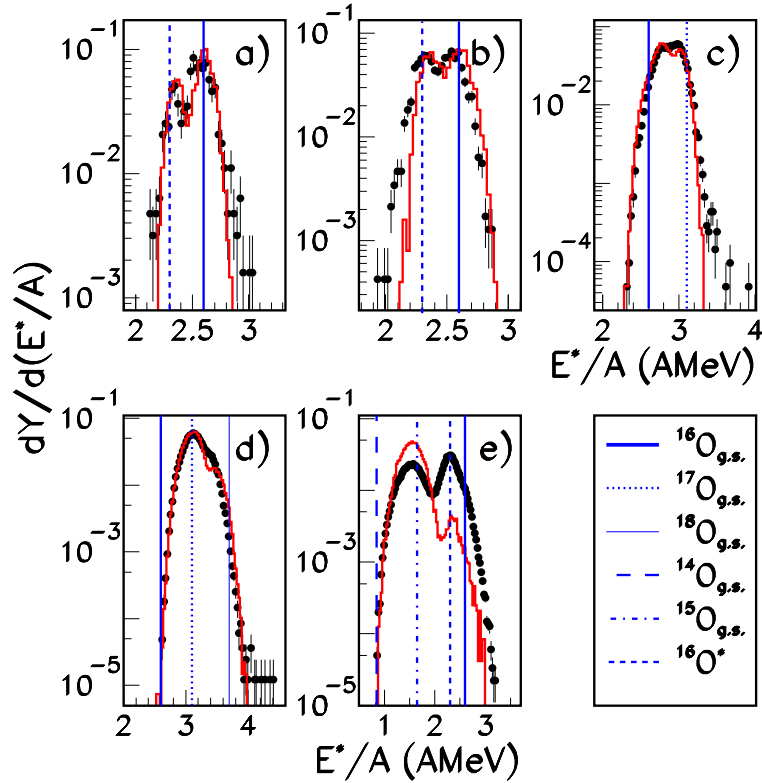


**Figure 11.** (Colour online) Calorimetric excitation energy distributions for the different channels associated with the production of an Oxygen residue: a)  $\text{O}+\alpha+2\text{d}$ ; b)  $\text{O}+\alpha+\text{p}+\text{t}$ ; c)  $\text{O}+\alpha+\text{p}+\text{d}$ ; d)  $\text{O}+\alpha+2\text{p}$ ; e)  $\text{O}+2\alpha$ . Full symbols: experimental data; (red) lines: HF $\ell$  calculations. Blue vertical lines: expected values for the ground (excited) states of different isotopes, as listed in the bottom right panel. Data and calculations are normalized to unitary area.

#### 403 4.2. Calorimetry and isotopic distributions

404 A deeper understanding of the reaction mechanism and a complementary test of the  
 405 statistical behaviour can be obtained by studying the mass distribution of the different  
 406 residues. Unfortunately we do not have isotopic resolution for fragments with atomic  
 407 number  $Z \geq 5$ . However, if we consider in the analysis events completely detected in  
 408 charge, the residue mass can be evaluated from the energy balance of the reaction, as  
 409 we now explain.

410 Let us consider a well defined channel, characterized by a given residue charge  
 411  $Z_{res}$ , light charged particle charge  $Z_{lcp} = 12 - Z_{res}$  and mass  $A_{lcp}$ . We define  
 412  $\bar{Q} = m_{lcp}c^2 - m(^{24}\text{Mg})c^2$  the *partial*  $Q$ -value associated with that channel, where  $m_{lcp}$  is  
 413 the total mass of the channel particles and  $m(^{24}\text{Mg})$  is the mass of the composite nucleus.  
 414 The unknown residue mass number  $A_{res}^k$  and unknown neutron number  $N_n^k$  in each event

415  $k$  belonging to the considered channel are defined as a function of an integer isotopic  
 416 variable  $x$  as  $A_{res}(x) = 2Z_{res} + x$  and  $N_n(x) = 24 - A_{lcp} - A_{res}(x) = 24 - A_{lcp} - 2Z_{res} - x$ .  
 417 The residue mass and total neutron energy are thus defined as a function of  $x$ :  
 418  $m_{res}(x) = m(A_{res}(x), Z_{res})$ ,  $E_n(x) = (\langle e_n \rangle + m_n c^2) N_n(x)$ , where  $\langle e_n \rangle$  is the estimate  
 419 of the average neutron kinetic energy from the average measured proton one, with the  
 420 subtraction of an average 2.9 MeV Coulomb barrier.

421 The excitation energy of the event  $k$  reads:

$$422 \quad E_{theo}^* = \bar{Q} + m_{res}(x) + E_{kin}^k + E_n(x) + E_\gamma^k \quad (8)$$

423 where  $E_{kin}^k$  is the total measured kinetic energy,  $E_{theo}^* = 62.4$  MeV the total available  
 424 energy, and  $E_\gamma^k$  the unmeasured  $\gamma$  energy, in the centre of mass system. The excitation  
 425 energy which would be associated to this event assuming that the residue has  $A_{res} =$   
 426  $2Z_{res}$  and is produced in its ground state is:

$$427 \quad E_{cal}(k) = \bar{Q} + m_{res}(x=0) + E_{kin}^k + E_n(x=0) \quad (9)$$

428 The example of Oxygen is reported in Figure 11. The calorimetric excitation energy  
 429 distribution  $E_{cal}(k)$  divided by the total mass of the system is displayed for the different  
 430 measured channels associated to the production of  $Z = 8$  fragments in complete events,  
 431 together with the filtered model calculations. In all cases we can observe a wide  
 432 distribution corresponding to different, often unresolved states of different isotopes. The  
 433 qualitative agreement with the model calculations confirms once again that the selected  
 434 events largely correspond to complete fusion.

435 In the hypothesis that the kinetic energies of LCP and neutrons depend on average  
 436 on the channel, but not on the average value of the residue mass (through  $\langle x \rangle$ ), (8)  
 437 and (9) can be averaged over the events of the channel giving:

$$E_{theo}^* = \bar{Q} + m_{res}(x) + \langle E_{kin} \rangle + E_n(x) + \langle E_\gamma \rangle \quad (10)$$

$$\langle E_{cal} \rangle = \bar{Q} + m_{res}(x=0) + \langle E_{kin} \rangle + E_n(x=0) \quad (11)$$

438 Eqs. (10) and (11) allow for deducing the unmeasured neutron excess, and therefore  
 439 the residue mass, from the average measured calorimetric energy. Indeed, subtracting  
 440 the two equations we get:

$$441 \quad \langle E_{cal} \rangle(x, I) = E_{theo}^* - (m_{res}(x) - m_{res}(x=0)) - (E_n(x) - E_n(x=0)) - E_I^* \quad (12)$$

442 This equation gives the calorimetric energy which is expected in average for a  
 443 residue of mass number  $A_{res} = 2Z_{res} + x$  produced in its excited state  $I$ , if we have  
 444 assumed via (9) that its mass number is  $2Z_{res}$ , as shown for various cases by the blue  
 445 vertical lines in Figure 11.

446 Our energy resolution is not sufficient to determine the detailed spectroscopy of  
 447 each residue, but the comparison of the measured calorimetric energy in each event  
 448 given by (9) with the expected value from (12) allows for a reasonably good isotopic  
 449 identification.

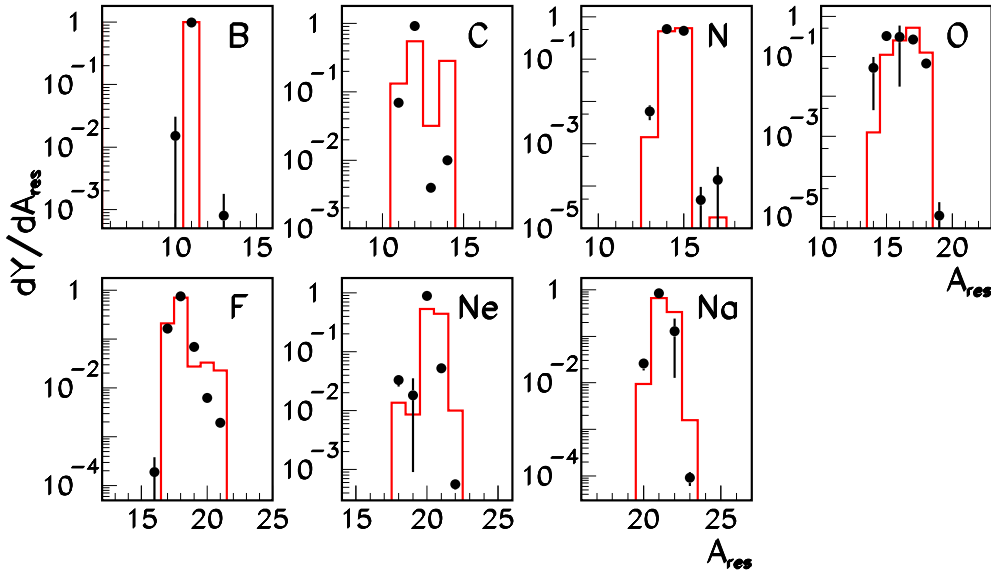


**Figure 12.** (Colour online) Experimental (symbols) isotopic distribution of residues obtained for complete events using (13) (see text), compared to theoretical predictions (histograms). Spectra are normalized to unitary area.

450 To attribute a definite isotope to each residue, we have minimized in each event  $k$  the  
 451 distance in energy between the calorimetric result and the theoretical value associated  
 452 to the resolved states of the associated channel

$$453 \quad |E_{cal}(k) - \langle E_{cal} \rangle(x, I)| = \min \quad (13)$$

454 We have repeated the same procedure for all the residues. The resulting isotopic  
 455 distributions are presented in Figure 12, again compared to the model calculations.  
 456 Errors on experimental results have been obtained combining the statistical error  
 457 with the one coming from the reconstruction procedure. This has been estimated by  
 458 comparing, within the model, the values obtained by the reconstruction procedure with  
 459 the original predictions. The global agreement is good, particularly for odd charge  
 460 residues. Both the average and the width of the distributions are reproduced by  
 461 the model. The distributions are generally bell-shaped and structureless, with the  
 462 exception of Carbon, which shows an important depletion for  $^{13}\text{C}$  similarly to the model  
 463 calculation.

464 The case of Oxygen is particularly interesting. The experimental and theoretical  
 465 widths are comparable, but while the experimental distribution has a negative skewness  
 466 and it is centered on the neutron poor  $^{15}\text{O}$ , the opposite is seen in the calculation which  
 467 favours neutron rich isotopes and presents a positive skewness [17]. As we can see in  
 468 Figure 11, this is largely due to the specific  $O + 2\alpha$  channel. Indeed this channel is the

only one which leads to a non-negligible production of  $^{15}\text{O}$ .

The information from the isotopic distribution and the energy spectra coherently points towards an increased probability for the  $O + 2\alpha$  channel with respect to the statistical model. We therefore turn to see if the experimental sample contains, together with a dominant contribution of standard compound reactions, other reaction mechanisms which could selectively populate a few specific channels, possibly associated with  $\alpha$  emission.

#### 4.3. Multiple $\alpha$ channels

In Table 1 we report for each residue the most populated channel in the experimental sample, as well as the associated branching ratio. The results are compared to the prediction of the statistical model for the same channel, filtered through the characteristics of the experimental apparatus. We can see that the branching ratio of the dominant decay channels is reasonably well reproduced by the statistical model for odd- $Z$  residues, while discrepancies can be seen for even- $Z$  ones.

$Z_{res}$	channel	$BR_{HF\ell}$	$BR_{EXP}$
5	$^{11-xn}B+xn+p+3\alpha$	100%	99%
6	$^{12-xn}C+xn+3\alpha$	66%	98%
7	$^{15-xn}N+xn+p+2\alpha$	94%	91%
8	$^{16-xn}O+xn+2\alpha$	11%	63%
9	$^{19-xn}F+xn+p+\alpha$	87%	92%
10	$^{22-xn}Ne+xn+2p$	84%	55%

**Table 1.** For each measured residue, the table gives the most probable experimental channel and its branching ratio together with the value predicted by the HF $\ell$  calculations. Errors on the experimental values (about 5%) take into account both the statistical error and the possible  $^3\text{He}$ - $\alpha$  contamination.

For Oxygen, the predicted most probable channel is  $^A\text{O}+\alpha+2H$  (here 2H stands for two  $Z=1$  products) with a branching ratio  $BR_{HF\ell} = 88\%$ , while this channel is experimentally populated with  $BR_{EXP} = 37\%$ . For Carbon,  $^{12}\text{C}+3\alpha$  is the most probable theoretical channel consistent with the data, but an important contribution of the channel  $^{12}\text{C}+2\alpha+2H$  is also predicted ( $BR_{HF\ell} = 32\%$ ), while this contribution is negligible in the experimental sample. Also for Neon a disagreement is present, but the theoretical calculation well reproduces the shape of the  $\alpha$  spectrum, as shown in Figure 9. This is not the case for Oxygen and, to a lesser extent, Carbon. For these residues the discrepancy in the branching ratios affects the shape of the  $\alpha$  particle spectra. This is shown in Figure 13, where, for the Carbon case (upper panels), the measured inclusive  $\alpha$  spectrum is dominated by the multiple  $\alpha$  channel, while in the statistical model the channel containing only two  $\alpha$  particles (and hence two hydrogen

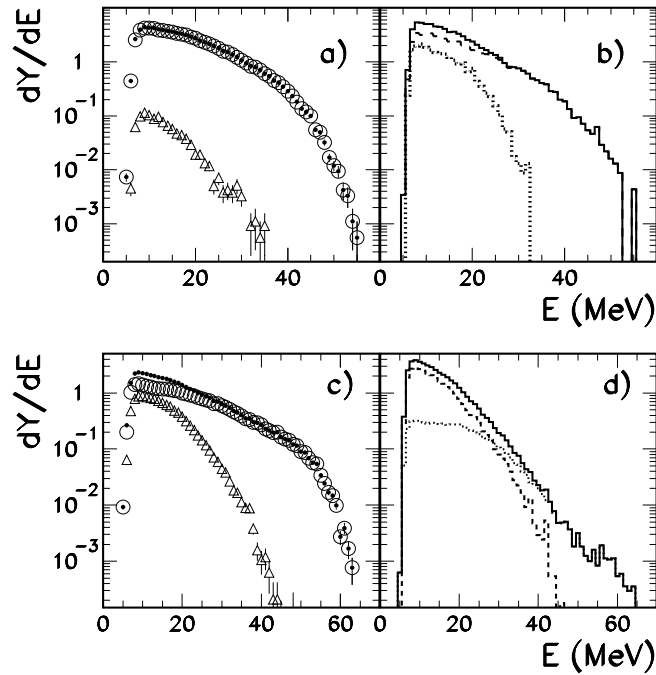


**Figure 13.** Experimental energy spectra (left) compared to HFℓ calculations (right). Upper part: Carbon residue: full symbols and full line represent the inclusive distribution of all decay channels, open triangles and dashed line correspond to channels involving two  $\alpha$ 's and two hydrogens, open circles and dotted line correspond to the three  $\alpha$ 's channel. Lower part: Oxygen residue: Full symbols and full line represent the inclusive distribution of all decay channels, open triangles and dashed line correspond to  $O + \alpha + 2H$  channel and open circles and dotted line correspond to  $O + 2\alpha$  channel. The spectra are normalized to the number of events of each residue.

495 isotopes) is very important for low  $\alpha$  energies, thus modifying the slope of the inclusive  
 496 spectrum with respect to the data.

497 A similar analysis for Oxygen is presented in Figure 13 (lower panels). The same  
 498 considerations as for Carbon apply in this case. Again, the extra yield associated with  
 499 multiple  $\alpha$  events with respect to the statistical model leads to a broader spectrum  
 500 extending towards higher  $\alpha$  energies.

501 If we now compare experimental data with model predictions in specific channels, we  
 502 obtain, for the Carbon case (see Figure 14, upper panels), that the shape of the spectra  
 503 of the different channels are very well reproduced by the statistical model calculations.  
 504 The same holds true for the angular distributions, well reproduced by calculations. This  
 505 shows that the kinematics of the decay is well described by a sequential evaporation  
 506 mechanism. However these shapes depend on the channel, multiple  $\alpha$ 's leading to  
 507 spectra which are less steep and extend further in energy, with respect to channels

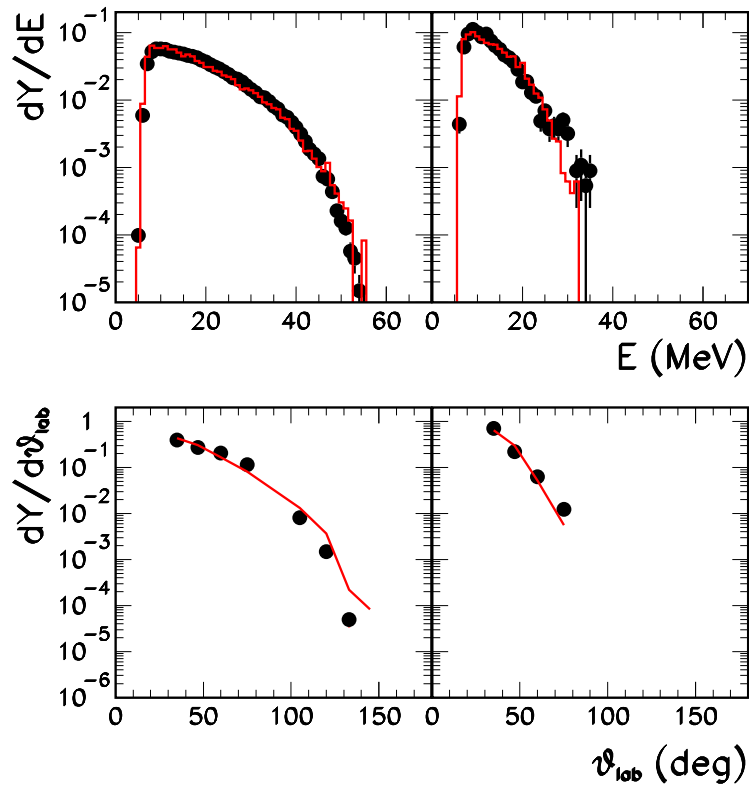


**Figure 14.** (Colour online) Energy spectra (upper panels) and angular distributions (lower panels) of  $\alpha$ -particles detected in coincidence with a Carbon residue. Data (symbols) are compared to HF $\ell$  calculations (lines) for the two channels  $C + 3\alpha$  (left) and  $C + 2\alpha + 2H$  (right). All the spectra are normalized to unitary area in order to compare the shapes independently of the different branching ratios.

508 where hydrogens are also present. Because of that, the disagreement in branching ratios  
 509 between model and data shown in Table I affects the global shape of the  $\alpha$  spectrum,  
 510 where the different channels are summed up.

511 Taking now into account the Oxygen residue, in Figure 15 we show the comparison  
 512 of the energy spectra (upper panels) and angular distributions. At variance with the  
 513 Carbon case, the shape of the  $\alpha$  spectrum and the angular distribution in the  $O + 2\alpha$   
 514 channel are not well reproduced by the statistical model. This means that the kinematics  
 515 in this channel is not compatible with CN decay, and suggests a contamination from  
 516 direct reactions.

517 The anomalously high probability of multiple  $\alpha$  emission in coincidence with  
 518 Oxygen and Carbon residues, with respect to the expectation from a statistical  
 519 behaviour, can explain the deviations observed in the inclusive  $\alpha$  observables (see  
 520 Figures 6 and 7). This suggests that non-statistical processes are at play in the

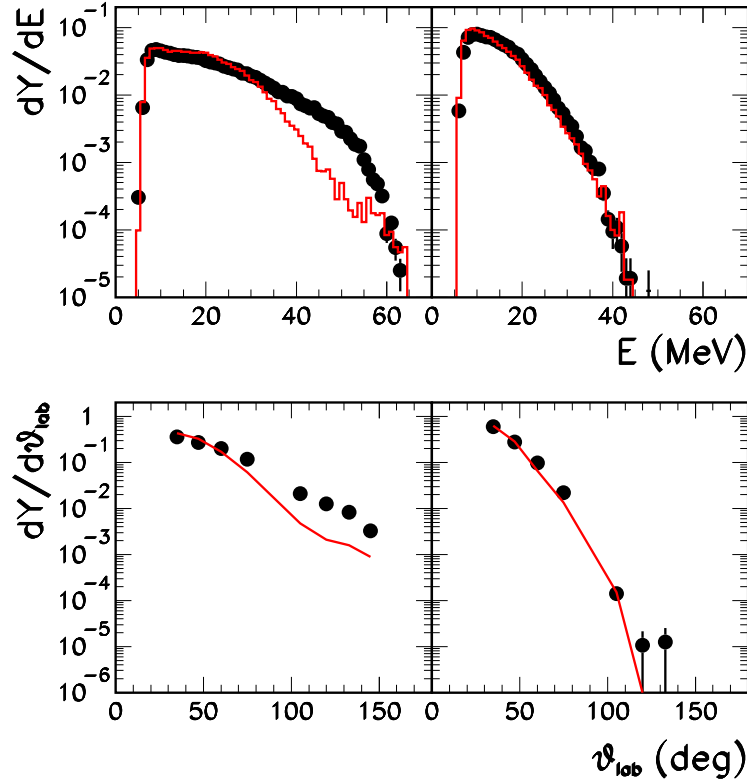


**Figure 15.** (Colour online) Energy spectra (upper panels) and angular distributions (lower panels) of  $\alpha$ -particles detected in coincidence with an Oxygen residue. Data (symbols) are compared to HF $\ell$  calculations (lines) for the two channels  $O + 2\alpha$  (left) and  $O + \alpha + 2H$  (right). All the spectra are normalized to unitary area in order to compare the shapes independently of the different branching ratios.

521 experimental sample concerning the two specific multiple  $\alpha$  channels that show  
 522 anomalously high branching ratios.

523 Alpha production is known to be an important outcome of direct  $^{12}\text{C}+^{12}\text{C}$   
 524 reactions [33, 34]. In these studies, though at lower bombarding energy than the present  
 525 experiment, the  $\alpha$  dominance has been associated with quasi-molecular two-Carbon  
 526 excited states with a pronounced  $\alpha$  structure.

527 In order to see if similar effects still persist at higher bombarding energies, in the  
 528 second paper of the series we will focus on a detailed analysis of the multiple  $\alpha$  channels.

## 529 5. Conclusions

530 In this work we have presented results for the  $^{12}\text{C}(^{12}\text{C},X)$  reaction at 95 MeV beam  
 531 energy, measured at LNL-INFN with the GARFIELD+RCo experimental set-up.

532 Starting from a minimal selection of the fusion-evaporation mechanism, based on  
 533 the coincidence between LCP's emitted over a wide polar angle range (GARFIELD)  
 534 and a fragment detected at laboratory forward angles (RCo), reinforced by completeness  
 535 conditions on the total detected charge and longitudinal momentum, we have compared  
 536 experimental data to statistical model calculations for the decay of the  $^{24}\text{Mg}^*$  CN issued  
 537 in case of complete fusion.

538 The selected sample is compatible with the expected behaviour of a complete-  
 539 fusion-evaporation reaction, with the exception of two specific channels significantly  
 540 more populated than predicted by the HF $\ell$  calculations. These channels correspond  
 541 to the emission of two or three  $\alpha$  particles in coincidence with an Oxygen or Carbon  
 542 residue, respectively. The  $\alpha$  spectra and angular distributions in the  $(O + 2\alpha)$  channel  
 543 are not compatible with statistical model calculation. This suggests a contamination  
 544 from direct reactions or  $\alpha$ -structure correlations in the  $^{24}\text{Mg}$  compound [35].

545 This is not the case for the  $(C + 3\alpha)$  channel, and the anomalously high branching  
 546 ratio of this channel can be tentatively attributed to a possible persistence at high  
 547 excitation energy of  $\alpha$  structure correlations in the  $^{12}\text{C}+^{12}\text{C}$  molecular state and/or in  
 548 the  $^{24}\text{Mg}$  compound. The kinematic characteristics of these non-statistical decays are  
 549 further studied in the continuation of this work [36].

550 The results of the analysis show that our data can be used to constrain the  
 551 ingredients of the statistical model in the  $A \leq 24$ ,  $E^* \leq 2.6$  AMeV mass-excitation-  
 552 energy region of interest.

553 In particular, this analysis supports a model showing a very steep increase of the  
 554 level density with excitation energy. The value of the level density parameter around  
 555 3 AMeV excitation energy extracted from this study is consistent with early findings  
 556 from fragmentation experiments.

## 557 Acknowledgments

558 The authors thank the crew of the XTU TANDEM acceleration system at LNL.  
 559 This work was partially supported by the European Funds for Large Scale Facilities  
 560 - Seventh Framework Program - ENSAR 262010 and by grants of Italian Ministry of  
 561 Education, University and Research under contract PRIN 2010-2011.

## 562 References

- 563 [1] Ghoshal S N 1950 *Phys. Rev.* **80** 939.  
 564 [2] Alhassid Y, Bertsch G F and Fang L 2003 *Phys. Rev. C* **68** 044322; Nakada H and Alhassid Y,  
 565 2008 *Phys. Rev. C* **78** 051304(R); Alhassid Y *et al Preprint* nucl-th/13047258.  
 566 [3] Guttormsen M *et al* 2003 *Phys. Rev. C* **68** 064306; Nyhus H T *et al* 2012 *Phys. Rev. C* **85** 014323.  
 567 [4] Charity R *et al* 2003 *Phys. Rev. C* **67** 044611; Charity R J 2010 *Phys. Rev. C* **82** 014610.  
 568 [5] Canto L F *et al* 2006 *Phys. Rep.* **424** 1, and references therein.  
 569 [6] Adhikari S *et al* 2006 *Phys. Rev. C* **74** 024602.  
 570 [7] Von Egidy T and Bucurescu D 2005 *Phys. Rev. C* **72** 044311; Von Egidy T and Bucurescu D 2006  
 571 *Phys. Rev. C* **73** 049901.



- 572 [8] Wiringa R B, Pieper S C, Carlson J and Pandharipande V R 2000 *Phys. Rev. C* **62** 014001;  
573 Kanada-Enyo Y and Horiuchi H 2001 *Prog. Theor. Phys. Suppl.* **142** 205; Neff T and Feldmeier  
574 H 2004 *Nucl. Phys. A* **738** 357.
- 575 [9] Ikeda K, Tagikawa N and Horiuchi H 1968 *Prog. Theor. Phys. Extra Suppl. (Jpn)* 464; Horiuchi  
576 H, Ikeda K and Kato K 2012 *Prog. Theor. Phys. Suppl.* **192** 1.
- 577 [10] J. A. Maruhn J A, M. Kimura M, S. Schramm S, P.-G. Reinhard P-G, H. Horiuchi H and A.  
578 Tohsaki A 2006 *Phys. Rev. C* **74** 044311; Reinhard P G, Maruhn J A, Umar A S and Oberacker  
579 V E 2011 *Phys. Rev. C* **83** 034312.
- 580 [11] Ebran J P, Khan E, Niksic T, Vretenar D 2012 *Nature* **487** 341-344.
- 581 [12] Matsumura H and Suzuki Y 2001 *Nucl. Phys. A* **739** 238; Yamada T and Schuck P 2004 *Phys.*  
582 *Rev. C* **69** 024309.
- 583 [13] Freer M 2007 *Rep. on Prog. in Phys.* **70** 2149.
- 584 [14] Costanzo E *et al* 1991 *Phys. Rev. C* **44** 111; Grenier F *et al* 2008 *Nucl. Phys. A* **811** 233; Raduta  
585 A R *et al* 2011 *Phys. Lett. B* **705** 65-70; Kokalova Tz, Itagaki N, von Oertzen W and Wheldon  
586 C 2006 *Phys. Rev. Lett.* **96** 192502; von Oertzen W *et al* 2008 *Eur. Phys. Journ. A* **36** 279; Di  
587 Pietro A *et al* *Journal of Physics: Conference Series* **366** 012013; Vardaci E *et al* 2013 *Journal*  
588 *of Physics: Conference Series* **436** 012054 and references quoted therein.
- 589 [15] Wallner A, Strohmeier B and Vonach H 1995 *Phys. Rev. C* **51**, 614.
- 590 [16] Baiocco G 2012 *PhD Thesis, Università di Bologna and Université de Caen Basse-Normandie*  
591 <http://amsdottorato.cib.unibo.it/4295/>
- 592 [17] Baiocco G *et al* 2013 *Phys. Rev. C* **87** 054614.
- 593 [18] Hauser W and Feshbach H 1952 *Phys. Rev.* **87** 366.
- 594 [19] Chen Z and Gelbke C K 1988 *Phys. Rev. C* **38** 2630.
- 595 [20] <http://www.chemistry.wustl.edu/rc/gemini++/>
- 596 [21] <http://www.nndc.bnl.gov/amdc/>
- 597 [22] <http://www.nndc.bnl.gov/nudat2/>
- 598 [23] Ignatyuk A V *et al* 1975 *Sov. J. Nucl. Phys.* **21** 255; Iljinov A S *et al* 1979 *Nucl. Phys. A* **543** 450.
- 599 [24] Toke J and Swiatecki W J 1981 *Nucl. Phys. A* **372** 141.
- 600 [25] Ricciardi M V *et al* 2004 *Nucl. Phys. A* **733** 299.
- 601 [26] Gramegna F *et al* *Nucl. Instrum. Methods A* **389** 474; Gramegna F *et al* 2004 *IEEE Nucl. Science*  
602 *Symposium, Rome IEEE Nucl. Sci. Symp. Conf. Proc.* **2** 1132; Moroni A *et al* 2006 *Nucl.*  
603 *Instrum. Methods A* **556** 516.
- 604 [27] Bruno M *et al* 2013 *Eur. Phys. Journ. A* **42** 128.
- 605 [28] Morelli L *et al* 2010 *Nucl. Instrum. Methods A* **620** 305.
- 606 [29] Rivet M F (*INDRA collaboration*) and De Filippo E (*CHIMERA collaboration*) - private  
607 communications.
- 608 [30] Bardelli L *et al* 2011 *Nucl. Instrum. Methods A* **654** 272; Carboni S *et al* 2012 *Nucl. Instrum.*  
609 *Methods A* **664** 251.
- 610 [31] Tarasov O. B. and Bazin D 2003 *Nucl. Instrum. Methods B* **204** 174.
- 611 [32] Gomez del Campo J *et al* 1979 *Phys. Rev. C* **19** 2170; Parks R L *et al* 1980 *Nucl. Phys. A* **348**  
612 350; Kovar G *et al* 1979 *Phys. Rev. C* **20** 1305; Sperr P *et al* 1976 *Phys. Rev. Lett.* **37** 321;  
613 Nambodiri M N *et al* 1976 *Nucl. Phys. A* **263** 491.
- 614 [33] Cosman E R *et al* 1975 *Phys. Rev. Lett.* **35** 265; Bremner C A *et al* 2002 *Phys. Rev. C* **66** 034605;  
615 Cormier T M, Jachcinski C M, Berkowitz G M, Braun-Munzinger P, Cormier P M, Gai M,  
616 Harris J W, Barrette J and Wegner H E 1978 *Phys. Rev. Lett.* **40** 924; Morsad A, Haas F, Beck  
617 C and Freeman R M 1991 *Z. Phys. A* **338** 61.
- 618 [34] Wuosmaa A H *et al* 1992 *Phys. Rev. Lett.* **68** 1295; Aliotta M *et al* 1995 *Z. Phys. A* **353** 43; Le  
619 Marechal R A *et al* 1997 *Phys. Rev. C* **55** 1881.
- 620 [35] Morelli L *et al* *Preprint nucl-ex/1309.0323 - Contribution to the 25th International Nuclear*  
621 *Physics Conference (INPC 2013), Firenze, Italy.*
- 622 [36] Morelli L *et al* submitted to *J. Phys. G: Nucl. Part. Phys.* .